Proceedings of the Seventh International Conference on
Railway Technology: Research, Development and Maintenance
Edited by: J. Pombo
Civil-Comp Conferences, Volume 15, Paper 3.5
Civil-Comp Press, Edinburgh, United Kingdom, 2026
ISSN: 2753-3239, doi: 10.4203/ccc.15.3.5

Temperature Field Reconstruction in Railway Wheel at Tread Braking via Adjoint-Based Heat Flux Identification

M. De Lara Todt, E. Landström Voortman,
R. Lundén and T. Vernersson

Department of Mechanical Engineering/CHARMEC, Chalmers University of Technology, Gothenburg, Sweden

Abstract

Non-uniform heating during tread braking leads to complex thermomechanical loading conditions and damage mechanisms. Replicating these effects numerically is challenging because the heat flux at the wheel–brake block interface cannot be measured directly and must instead be inferred from temperature data. To address this, the present work introduces an adjoint-based inverse heat transfer method to reconstruct the transient temperature field on a railway wheel tread subjected to prolonged drag braking. The braking heat flux is parameterized using a truncated Fourier series in the circumferential direction and a sinusoidal lateral bias across the tread. The coefficients are calibrated by minimizing the discrepancy between simulated and measured mid-tread temperatures from a brake-roller test rig. The inverse problem is formulated as a PDE-constrained optimization problem and solved efficiently using an adjoint method with checkpointing, enabling gradient-based optimization over long braking durations. The reconstructed temperature fields show good agreement with mid-tread measurements at multiple braking times, capturing the dominant circumferential temperature variations and providing a consistent basis for analyzing thermal localization under tread braking conditions.

Keywords: railway wheels, tread braking, heat transfer, hot spots, thermal localization, inverse problems

1 Introduction

Tread braking is the most common braking system used in freight wagons, narrow-gauge railway vehicles, and slow passenger cars, due to its low complexity and cost, ease of maintenance, and compatibility with underframe clearance constraints. However, the interfacial friction from braking leads to substantial tread heating, subjecting the rolling contact surface to high temperatures in combination with normal and tractive forces [1].

In both heavy haul railway applications and brake rig tests, it has been observed that heating may not be circumferentially uniform [2]. Due to irregularities in the wheel tread and brake block surfaces, the contact pressure during braking becomes uneven, resulting in spatially heterogeneous temperature distributions. This phenomenon, characterized by localized hot spots, has been referred to as ThermoElastic Instabilities (TEI) in the literature [3, 4]. In addition, a distinct form of non-uniform heating, known as Thermal Localization (TL), has also been reported [5–7]. In contrast to TEI, TL is associated with a more global variation of temperature along the wheel tread circumference. It has been suggested that TL may originate from wheel out-of-roundness and can significantly influence material plastification and residual stress development, potentially leading to thermal cracking [8].

In this context, accurate numerical prediction of transient temperature fields in railway wheels during braking is essential for analyzing thermomechanical loading and predicting residual stresses, as these can contribute to damage mechanisms such as thermal cracking and rolling contact fatigue. While finite element models can accurately describe heat diffusion within the wheel, their predictive capability depends strongly on the specification of the thermal boundary conditions, particularly the heat flux at the contact interface, which cannot be measured directly in experimental conditions [9]. As a result, prescribing realistic temporally and spatially varying heat fluxes remains a major challenge.

To address this limitation, the present work formulates the problem as the identification of an unknown heat flux together with the reconstruction of measured surface temperatures in a numerical model implemented in the commercial finite element software ABAQUS [10]. The heat flux is treated as a control variable that enables the numerical solution to match the measured temperatures. This leads to an inverse heat transfer problem formulated as a PDE-constrained optimization, in which the discrepancy between simulated and measured temperatures is minimized by adjusting a suitable parametrization of the boundary heat flux.

Inverse heat transfer problems are known to be ill-posed and sensitive to measurement noise, which requires the use of regularization and efficient numerical strategies [11]. Among the available approaches, adjoint-based optimization methods pro-

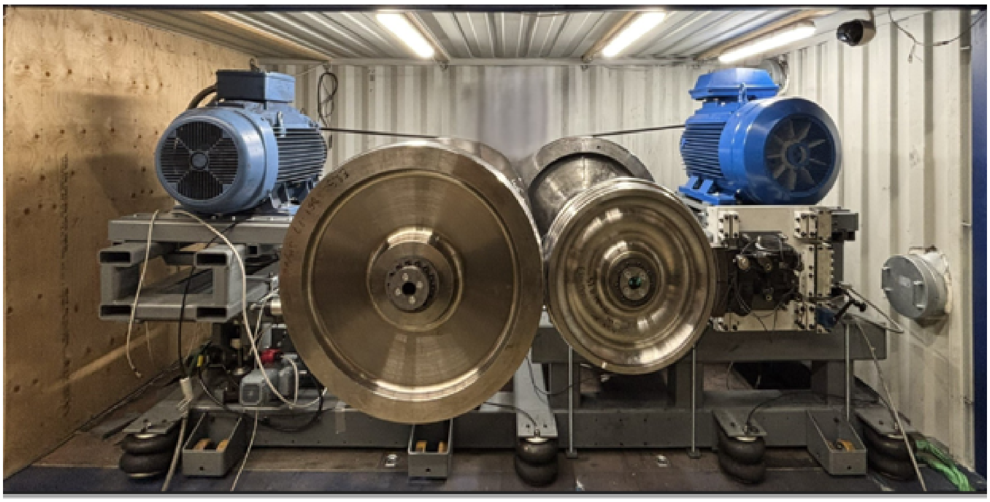

Figure 1: The CHARMEC Brake Roller Rig at Chalmers University of the Technology. The rail-wheel module with the motor controlling traction is visible on the left, with the test wheel and the driving motor seen on the right.

vide an efficient framework, as they allow the computation of gradients of the cost functional with respect to a large number of parameters at a computational cost that is largely independent of the parameter dimension [12].

In this paper, we present a temperature-field reconstruction framework that combines a Fourier-based parametrization of the boundary heat flux with an adjoint-based optimization method to efficiently solve the associated PDE-constrained optimization problem. The methodology is validated using experimental temperature measurements obtained from rig tests. The reconstructed heat flux is not considered a primary physical quantity of interest but rather a control input that enables the numerical model to reproduce the experimentally observed thermal response.

2 Experimental data

The experimental data used in the present study are from a previously published test campaign [5] conducted at Chalmers University of Technology, using the in-house-designed CHARMEC Brake Roller Rig shown in Figure 1. Although the test facility is capable of testing under combined normal load, traction load, axial displacement, and various braking configurations, the data adopted here correspond exclusively to tread braking tests conducted at approximately constant braking power levels, without engaging the rail-wheel module.

Forced ventilation is employed to avoid overheating of the surrounding components. The test rig enables testing under controlled drag braking conditions at constant speed, allowing, nominally, reproducible thermal loading of the wheel.

The brake system consists of a single composite brake block actuated by a pneumatic system and a 4th-generation BFC tread brake unit (provided by Wabtec Faiveley Nordic). The unit is mounted on a support device that allows the mounting stiffness to be adjusted by replacing internal springs, thereby enabling control of the compliance of the BFC unit and the brake block. In the referenced test campaign, constant braking power levels of 30, 40, and 50 kW are applied to generate representative thermal loading conditions.

To investigate the effect of non-uniform heating, the temperature field is measured using a high-speed thermographic system together with a sliding thermocouple in contact with the wheel tread. A FLIR X6541sc infrared camera, equipped with an indium antimonide (InSb) detector operating in the 2–5 µm wavelength range, is employed and configured to record a sub-window of 8×320 pixels, at frame rates between 2000 and 3000 Hz depending on the test conditions. The camera does not observe the wheel tread directly; instead, a mirror is used to redirect the view of the tread toward the camera.

During the tests, wear of the brake blocks generates dust particles that progressively deposit on the mirror surface, reducing the amount of mid-wave infrared radiation reaching the detector and, consequently, leading to an underestimation of the measured temperature. To mitigate this effect, the mirror is periodically cleaned throughout the experiments. In addition, during data post-processing, the thermocamera measurements are corrected by matching their spatially averaged temperature to the corresponding averages obtained from the thermocouple, thus compensating for both changes in tread emissivity and dust on the mirror surface. Figure 2a illustrates the influence of mirror dust on the average temperatures measured by the thermocamera, while Figure 2b shows an example of the calibration procedure applied to the thermocamera data.

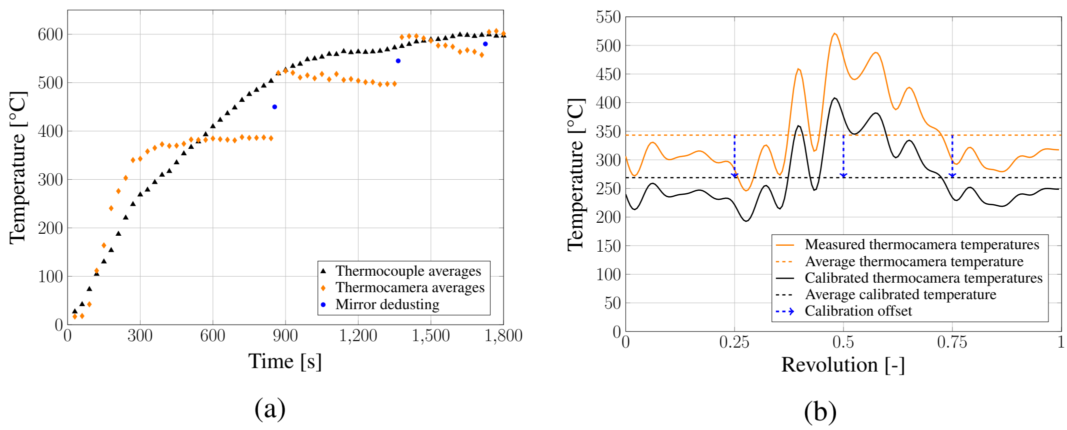

Figure 2: Calibration of the thermocamera measurements. (a) Evolution of thermocamera and thermocouple average temperatures at 30 kW testing. (b) Measured and calibrated thermocamera temperatures over one revolution after 300 s of braking.

3 Numerical implementation

We formulate the inverse problem as a PDE-constrained optimization problem, in which the boundary heat flux $q(\mathbf{X}, \boldsymbol{\theta}, t)$ is identified by minimizing the discrepancy between simulated and measured temperatures, while enforcing the transient heat conduction equation as a constraint.

Thus, the optimization problem reads

$$\min J(\boldsymbol{\theta}) := \frac{1}{2} \left\| T(\mathbf{X}, \boldsymbol{\theta}, t) - T_{\text{obs}}(\mathbf{X}, t) \right\|^2_{L^2(\Gamma_{\text{t}})} + \frac{1}{2} \mathcal{R}(\boldsymbol{\theta}, t), \tag{1}$$

subjected to the state equation

$$\begin{aligned}
\rho c_{\text{p}} \frac{\partial T}{\partial t} &= \nabla \cdot (\kappa \nabla T), && \text{in} \quad \Omega \times (0, t_{\text{f}}], \\
T(\mathbf{X}, \boldsymbol{\theta}, \mathbf{0}) &= T_0(\mathbf{X}), && \text{in} \quad \Omega \\
-\kappa \frac{\partial T}{\partial \hat{\mathbf{n}}} &= h(T_\infty - T) + \epsilon\sigma(T_\infty^4 - T^4), && \text{on} \quad \Gamma_{(\text{f,r,w})} \times (0, t_{\text{f}}] \\
-\kappa \frac{\partial T}{\partial \hat{\mathbf{n}}} &= q(\mathbf{X}, \boldsymbol{\theta}, t) + h(T_\infty - T) + \epsilon\sigma(T_\infty^4 - T^4), && \text{on} \quad \Gamma_{\text{t}} \times (0, t_{\text{braking}}] \\
-\kappa \frac{\partial T}{\partial \hat{\mathbf{n}}} &= h(T_\infty - T) + \epsilon\sigma(T_\infty^4 - T^4), && \text{on} \quad \Gamma_{\text{t}} \times (t_{\text{braking}}, t_{\text{f}}]
\end{aligned} \quad . \tag{2}$$

Throughout the whole simulation, convective and radiation are prescribed on the wheel's flange, rim, and web external surfaces $\Gamma_{(\text{f,r,w})}$. The surface Γ_{h} is assumed to be insulated. On the tread surface both the heat flux and the cooling terms are included, but the heat flux is applied only in the interval $t = (0, t_{\text{braking}}]$. After braking, $t = (t_{\text{braking}}, t_{\text{f}}]$, only radiation and convection are applied on the tread. Figure 3 displays a graphical representation of the wheel's boundary partitions. We must note that rail-chilling effects are not being considered in this model since the experiments did not utilize the rail wheel.

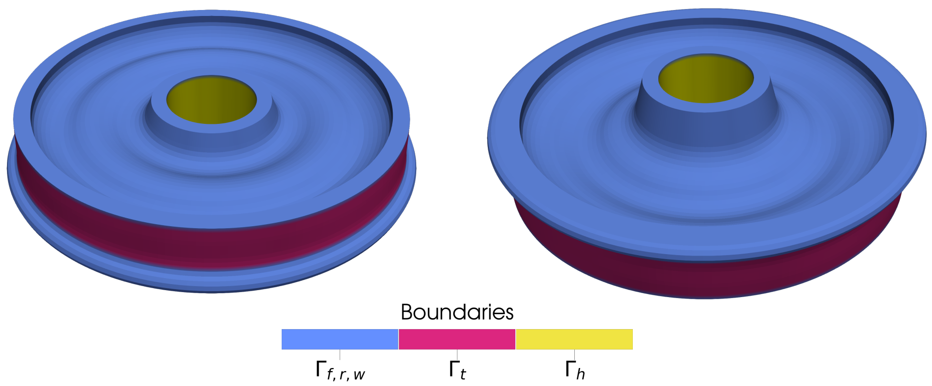

Figure 3: Partitions of the wheel's boundary.

The film coefficients for convection are defined through a FILM Fortran subroutine in Abaqus, based on the empirical formulae present in [13], and the emissivity for radiation is assumed to be

$$\epsilon = \begin{cases} \epsilon_{\mathrm{t}} = 0.65, & \text{on } \Gamma_{\mathrm{t}} \\ \epsilon_{(\mathrm{f,r,w})} = 0.95, & \text{on } \Gamma_{(\mathrm{f,r,w})} \end{cases}.$$

The material is assumed to have a constant density ρ of 7850 kg/m^3. However, the thermal conductivity κ and the specific heat c_p are adjusted multilinearly with the change in temperature such that

$$c_{\mathrm{p}} = c_{\mathrm{p}}(T), \quad \text{and} \quad \kappa = \kappa(T),$$

according to the data in Table 1.

Table 1: Material thermal properties.

Temperature T [ºC]	Conductivity κ [W/(m $\cdot$ K)]	Specific Heat c_{p} [J/(kg $\cdot$ K)]
0	43.7	440
200	44.1	510
400	39.3	570
600	32.9	630
800	25.0	700

The misfit term measures the difference between the numerical temperature field $T(\mathbf{X}, \boldsymbol{\theta}, t)$ and the experimental observations $T_{\mathrm{obs}}(\mathbf{X}, t)$ on the tread surface over the time interval of interest. Restricting the comparison to Γ_{t} reflects the fact that measurements are only available on the tread and that the heat flux acts on this boundary.

The regularization term $\mathcal{R}(\boldsymbol{\theta})$ is introduced to mitigate the ill-posedness of the inverse heat transfer problem and to stabilize the identification of the heat flux. It penalizes non-physical or excessively oscillatory solutions and reduces sensitivity to measurement noise.

Based on previous studies [5, 6], we assume that both the tread temperature and heat flux are distributed periodically along the circumferential direction. Accordingly, the braking heat flux is expanded in a truncated Fourier-series as

$$q(\mathbf{X}, \boldsymbol{\theta}, t) = \sin\gamma \sum_{k=0}^{n-1} \left[\frac{a_k(t)}{A} \cos(\beta k) + \frac{b_k(t)}{A} \sin(\beta k) \right]. \tag{3}$$

Where, the implicit control variable vector is

$$\boldsymbol{\theta}(t) = [a_0(t), \ldots, a_{n/2-1}(t), b_0(t), \ldots, b_{n/2-1}(t)]^T \in \mathbb{R}^n,$$

with even n. Here, A denotes the braked area of the tread, and β is the Cartesian azimuth angle. In the lateral direction, we assume that hot spots form at the center of the tread and that the temperature decays sinusoidally towards both edges. This behavior is modeled by the factor $\sin\gamma$, which attains its maximum at the tread center. For the wheel geometry considered in this work, γ is defined as

$$\gamma = -\pi(12.5y + 0.125) \quad \text{[m]},$$

where $y = 0$ corresponds to the field side of the rim. The heat flux is implemented in the ABAQUS software using the DFLUX subroutine.

3.1 Adjoint equation

To efficiently compute the gradient of the cost functional with respect to a potentially large number of control parameters, the problem is rewritten using an adjoint formulation. A Lagrangian functional [14] is introduced to incorporate the governing heat equation as a constraint,

$$\mathcal{L}(T, \lambda, \boldsymbol{\theta}) = J(\boldsymbol{\theta}) + \int_0^t \int_\Omega \lambda \rho c_{\mathrm{p}} \frac{\partial T}{\partial t} d\Omega dt - \int_0^t \int_\Omega \lambda \nabla \cdot (\kappa \nabla T) d\Omega dt \tag{4}$$

Where $\lambda(\mathbf{X}, t)$ is the adjoint variable. The adjoint field arises as the Lagrange multiplier associated with the heat equation constraint and acts as a sensitivity field linking temperature variations to variations of the control parameters.

The stationarity of the Lagrangian with respect to arbitrary variations $\delta\lambda$ and δT, *i.e.*

$$\frac{\partial \mathcal{L}(T, \lambda, \boldsymbol{\theta})}{\partial \lambda} \delta\lambda = 0, \quad \text{and} \quad \frac{\partial \mathcal{L}(T, \lambda, \boldsymbol{\theta})}{\partial T} \delta T = 0,$$

yields, respectively, the heat equation (2), and the adjoint equation

$$\begin{aligned} -\rho c_{\mathrm{p}} \frac{\partial \lambda}{\partial t} &= \nabla \cdot (\kappa \nabla \lambda), \quad \text{in} \quad \Omega \times (0, t_{\mathrm{f}}], \\ \lambda(\mathbf{X}, t_{\mathrm{f}}) &= 0, \qquad \text{in} \quad \Omega \\ -\kappa \frac{\partial \lambda}{\partial \hat{\mathbf{n}}} &= -\lambda h - 4\lambda\epsilon\sigma T^3, \quad \text{on} \quad \Gamma_{(\mathrm{f,r,w})} \times (0, t_{\mathrm{f}}] \\ -\kappa \frac{\partial \lambda}{\partial \hat{\mathbf{n}}} &= (T - T_{\mathrm{obs}}) - \lambda h - 4\lambda\epsilon\sigma T^3, \quad \text{on} \quad \Gamma_{\mathrm{t}} \times (0, t_{\mathrm{f}}] \end{aligned}. \tag{5}$$

The implementation of Equation 5 in ABAQUS is not straightforward for two main reasons. First, the adjoint problem is formulated backward in time, whereas the commercial finite element software ABAQUS is inherently designed to solve transient problems forward in time. Second, the material properties κ and c_{p}, and the cooling fluxes, depend on the temperature field T, which is not the solution variable of the adjoint problem but is instead obtained from the forward heat transfer analysis.

To deal with the first issue, we use the change of variables $\tau = t_\mathrm{f} - t$. For the second one, we introduce the starred material properties to account for the temperature dependence of the thermal coefficients,

$$c_\mathrm{p}^* = c_\mathrm{p}(T^*), \quad \text{and} \quad \kappa^* = \kappa(T^*).$$

Where T^* is the temperature field solution at the centroid of the elements from the forward problem. For the cooling fluxes, the same process is taken. This approach reduces the amount of data that needs to be saved from the forward solving. The correction for the starred property variables is made by using the UMATH subroutine, and the correction for fluxes is implemented using the DFLUX subroutine.

Both implementations result in the adjoint equation

$$\begin{aligned} \rho c_\mathrm{p}^* \frac{\partial \lambda}{\partial \tau} &= \nabla \cdot (\kappa^* \nabla \lambda), && \text{in} \quad \Omega \times (0, t_\mathrm{f}], \\ \lambda(\mathbf{X}, 0) &= 0, && \text{in} \quad \Omega \\ -\kappa^* \frac{\partial \lambda}{\partial \hat{\mathbf{n}}} &= -\lambda h - 4\lambda\epsilon\sigma(T^*)^3, && \text{on} \quad \Gamma_{(\mathrm{f,r,w})} \times (0, t_\mathrm{f}] \\ -\kappa^* \frac{\partial \lambda}{\partial \hat{\mathbf{n}}} &= (T^* - T_\mathrm{obs}) - \lambda h - 4\lambda\epsilon\sigma(T^*)^3, && \text{on} \quad \Gamma_\mathrm{f} \times (0, t_\mathrm{f}] \end{aligned} . \tag{6}$$

Where $T^* = T^*(\mathbf{X}, t_\mathrm{f} - \tau)$, and $T_\mathrm{obs} = T_\mathrm{obs}(\mathbf{X}, t_\mathrm{f} - \tau)$.

3.2 Gradient computation

By solving both the state (2) and adjoint (6) equations we can compute the gradients of the cost function in the $\delta\boldsymbol{\theta}$ direction

$$\frac{\partial \mathcal{L}(T, \lambda, \boldsymbol{\theta})}{\partial \boldsymbol{\theta}} \delta\boldsymbol{\theta} = -\int_0^{t_f} \int_{\Gamma_t} \lambda \frac{\partial q}{\partial \boldsymbol{\theta}} \delta\boldsymbol{\theta} ds dt + \frac{\partial \mathcal{R}}{\partial \boldsymbol{\theta}} \delta\boldsymbol{\theta}. \tag{7}$$

In the discrete sense, Equation 7 can be written as

$$\mathbb{R}^n \ni \nabla_{\boldsymbol{\theta}} J = -\mathbf{G}^T \boldsymbol{\lambda} + \nabla_{\boldsymbol{\theta}} \mathcal{R}(\boldsymbol{\theta}), \tag{8}$$

where $\boldsymbol{\lambda} \in \mathbb{R}^m$ is the adjoint solution vector evaluated at the m discrete space-time points on Γ_t, *i.e.* the nodes, and $\mathbf{G} \in \mathbb{R}^{m \times n}$ is the Jacobian of the heat flux with respect to the n control parameters,

$$\mathbf{G} = \frac{\partial q(\mathbf{X}, \boldsymbol{\theta}, t)}{\partial \boldsymbol{\theta}} = \begin{bmatrix} \frac{\partial q(\mathbf{X}_1, \boldsymbol{\theta}, t)}{\partial \boldsymbol{\theta}_1} & \frac{\partial q(\mathbf{X}_1, \boldsymbol{\theta}, t)}{\partial \boldsymbol{\theta}_2} & \cdots & \frac{\partial q(\mathbf{X}_1, \boldsymbol{\theta}, t)}{\partial \boldsymbol{\theta}_n} \\ \frac{\partial q(\mathbf{X}_2, \boldsymbol{\theta}, t)}{\partial \boldsymbol{\theta}_1} & \frac{\partial q(\mathbf{X}_2, \boldsymbol{\theta}, t)}{\partial \boldsymbol{\theta}_2} & \cdots & \frac{\partial q(\mathbf{X}_2, \boldsymbol{\theta}, t)}{\partial \boldsymbol{\theta}_n} \\ \vdots & \vdots & \ddots & \vdots \\ \frac{\partial q(\mathbf{X}_m, \boldsymbol{\theta}, t)}{\partial \boldsymbol{\theta}_1} & \frac{\partial q(\mathbf{X}_m, \boldsymbol{\theta}, t)}{\partial \boldsymbol{\theta}_2} & \cdots & \frac{\partial q(\mathbf{X}_m, \boldsymbol{\theta}, t)}{\partial \boldsymbol{\theta}_n} \end{bmatrix} = \begin{bmatrix} \mathbf{G}_{1,:} \\ \mathbf{G}_{2,:} \\ \vdots \\ \mathbf{G}_{m,:} \end{bmatrix}.$$

For the braking heat flux used in this work, Equation 3,

$$\mathbf{G}_{k,:} = \frac{\sin\gamma_k}{A}\left[1, \cos(\beta_k), \ldots, \cos((n/2-1)\beta_k), 0, \sin(\beta_k), \ldots, \sin((n/2-1)\beta_k)\right].$$

Hence, the computation of the Jacobian is analytical and does not require forward or adjoint results.

For the regularization term, we use a Tikhonov regularization [11], thus

$$\mathcal{R}(\boldsymbol{\theta}) = \frac{\alpha}{2}\left\|\boldsymbol{\theta}\right\|_2^2. \tag{9}$$

With α being the Tikhonov regularization parameter. This leads to

$$\nabla_{\boldsymbol{\theta}}\mathcal{R}(\boldsymbol{\theta}) = \alpha\boldsymbol{\theta}.$$

3.3 Checkpoint strategy and optimization workflow

Due to the long duration of drag braking tests and the high temporal resolution of the measurements, solving the inverse problem over the full interval $[0, t_{\text{braking}}]$ would require storing a very large amount of forward data for the adjoint computation, leading to high memory and I/O costs [12].

To address this, a checkpoint strategy is adopted. The braking interval is divided into N_c smaller sub-intervals,

$$[0, t_{\text{braking}}] = \bigcup_{i=1}^{N_c}[t_{i-1}, t_i],$$

and an independent inverse problem is solved on each checkpoint. This limits the amount of forward data that must be stored at a time.

At the beginning of each checkpoint, the temperature field is taken from the forward solution of the previous interval and used as the initial condition. The temporally constant heat flux is then identified only within the studied sub-interval. After the last checkpoint, *i.e.* for $(t > t_{\text{braking}})$, the heat flux is set to zero and only cooling by convection and radiation is applied.

For each checkpoint, the minimization of the local cost functional is performed using a gradient-based BFGS algorithm with Armijo line-search conditions [15]. The gradient is computed from the adjoint solution as

$$\nabla_\theta J_i = -\mathbf{G}^T\boldsymbol{\lambda}_i + \alpha\boldsymbol{\theta}_i, \tag{10}$$

and is used to update the control parameters until convergence.

This checkpoint strategy makes the adjoint-based optimization computationally feasible for the here considered long drag-braking events with high-resolution thermal data, while ensuring stable and efficient convergence of the inverse heat flux identification. Algorithm 1 shows the structure of the method.

Algorithm 1: Checkpoint-based optimization workflow

Input: T_{obs}, $\boldsymbol{\theta}_0$, α, ξ
Output: $\boldsymbol{\theta}_i$ for each checkpoint
Divide the braking interval $[0, t_{\text{braking}}]$ into N_c checkpoints $[t_{i-1}, t_i]$;
Assemble the Jacobian matrix $\mathbf{G}$ from the Fourier basis;
for $i = 1, \ldots, N_c$ **do**
    Initialize $\boldsymbol{\theta}_i$;
    while $||\nabla_\theta J|| \geq \xi$ **do**
        Solve the forward problem (2) on $[t_{i-1}, t_i]$ and store T^*;
        Solve the adjoint problem (6) on $[t_{i-1}, t_i]$;
        Compute the gradients (10);
        Update $\boldsymbol{\theta}_i$ using BFGS with Armijo conditions;
Set $q(\mathbf{X}, \theta, t) = 0$ for $t = [t_{\text{braking}}, t_{\text{f}}]$ and continue the forward simulation using only cooling boundary conditions;

4 Results

Figure 4 compares the experimentally measured mid-tread temperatures along with those reconstructed using the inverse heat transfer method at three representative instants of braking, for the 30 kW brake-power test case. The inverse problem is solved using a Fourier-based parameterization of the circumferential heat flux with 60 modes (*i.e.* $n = 60$), together with an adjoint checkpoint strategy in which checkpoints are stored every 300 s, and the regularization parameter $\alpha = 1 \times 10^{-5}$.

The temperature profiles are shown as a function over a wheel revolution, highlighting the circumferential variations induced by the moving heat source on the wheel tread. Overall, the numerical reconstructions reproduce both the amplitude and phase of the experimental temperature distributions with good accuracy, indicating that the chosen heat-flux parameterization and optimization strategy are able to capture the dominant thermal features. Local discrepancies are observed at specific circumferential locations and time instants, which can be attributed to measurement noise not fully eliminated through regularization, as well as modeling assumptions such as the mid-section line geometrical representation of the heat-flux and the finite spatial resolution of the truncated Fourier series.

Figure 5 shows the reconstructed temperature fields at selected time steps during braking at 30 kW, now presented as an isometric view of the wheel (at the top) and as an unwrapped two-dimensional representation of the wheel exterior surfaces, *i.e.* tread and flange, (at the bottom). At 300 s, localized hotspots are clearly visible along the tread, with one circumferential region exhibiting higher temperatures than the rest of the wheel. At 900 s, as individual hotspots expand and begin to merge into larger high-temperature zones, distinct localized patterns form, leading to the emergence of a wheel hot-side and cold-side. At the final studied time instant, the temperature distribution becomes largely uniform around the circumference.

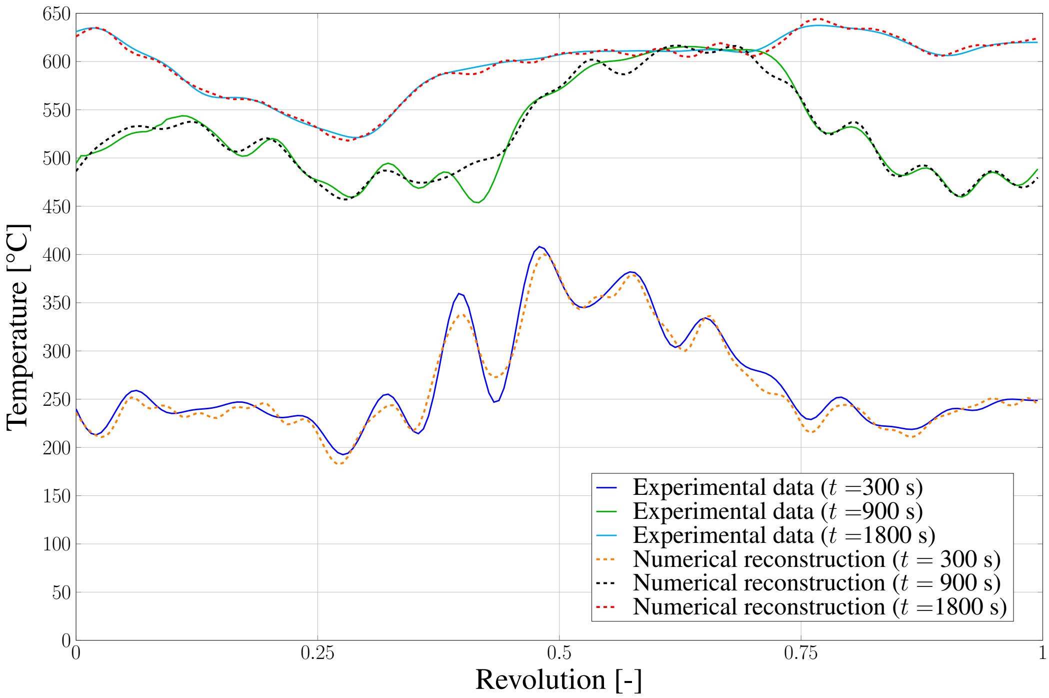

Figure 4: Comparison between experimentally measured and reconstructed mid-section temperatures at three representative braking times.

5 Concluding remarks

This work presented an adjoint-based inverse heat transfer framework for reconstructing transient temperature fields in a railway wheel subjected to prolonged tread braking. By parameterizing the circumferential heat flux using a truncated Fourier series and solving the resulting PDE-constrained optimization problem, the method was able to reproduce experimentally measured mid-tread temperatures with good accuracy at multiple instants during braking. The reconstructed temperature fields reproduce circumferential non-uniformities during braking, including hot spots and thermal localization.

The present inverse formulation identifies the heat flux based on temperature measurements along a mid-section line of the wheel tread, which provides a practical and computationally efficient first step. However, the adjoint-based framework employed in this work is not limited to this configuration. Future work will extend the methodology to identify a heat flux defined over the entire tread surface, allowing both circumferential and lateral variations of the heat input to be reconstructed simultaneously. Due to the favorable scaling properties of the adjoint method, this extension can be achieved without a prohibitive increase in computational cost and is expected to further improve the fidelity of the reconstructed temperature fields.

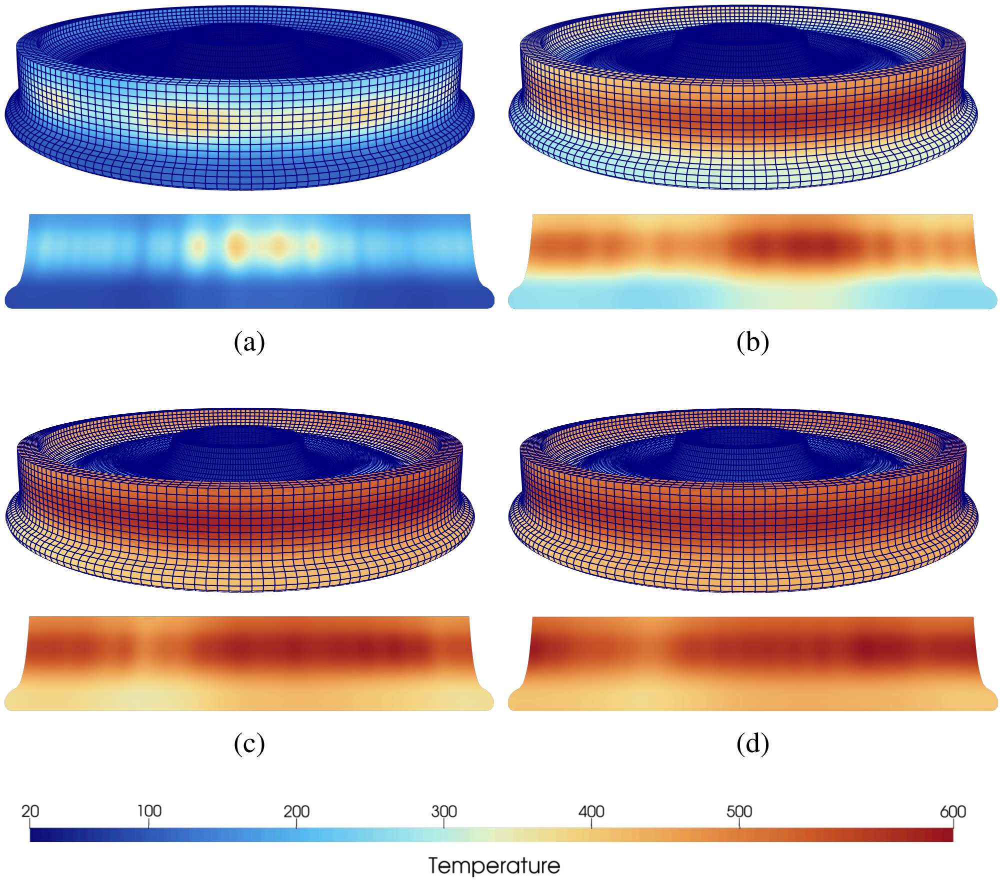

Figure 5: Reconstructed temperature fields at selected time steps during braking: (a) 300 s, (b) 900 s, (c) 1500 s, and (d) 1800 s. For each time instant, the top row shows an isometric view, while the bottom row presents an unwrapped representation of the circumferential temperature distribution.

Acknowledgements

This work is part of the activities within the Swedish National Centre of Excellence CHARMEC (Chalmers Railway Mechanics). The simulations were performed using resources at Chalmers Centre for Computational Science and Engineering (C3SE) provided by the National Academic Infrastructure for Supercomputing in Sweden (NAISS).

References

[1] K.L. Johnson, Contact mechanics, Cambridge University Press, 1987.

[2] R.C. Parker, P.R. Marshall, "The measurement of the temperature of sliding surface with particular reference to railway brake blocks", Proceedings Institution of Mechanical Engineers, 158:209–229, 1948.

[3] M.C. Fec, H. Sehitoglu, “Thermal-mechanical damage in railroad wheels due to hot spotting”, Wear, 102(1):31–42, 1985.
[4] J.R. Barber, T.W. Beamond, J.R. Waring, C. Pritchard, “Implications of thermoelastic instability in automotive disc brakes under a drag brake application”, ASME Journal of Tribology, 107:206–210, 1985.
[5] E.V. Landström, T. Vernersson, R. Lundén, “Analysis and testing of tread braked railway wheel-effects of hot spots on wheel performance”, International Journal of Fatigue, v. 180, p. 108116, 2024.
[6] E.V. Landström, T. Vernersson, R. Lundén, “Characterisation and evaluation of global uneven heating during railway tread braking–Brake rig testing and field study”, Proceedings of the Institution of Mechanical Engineers, Part F: Journal of Rail and Rapid Transit, v. 239, n. 3, p. 258-271, 2025.
[7] J. Cookson, P. Mutton, L. Tran, C. Qui, R. Saporito, G. Crew, ”Tread damage due to extreme thermal localization under high braking loads in heavy haul operations”, Proceedings of the 20th International Wheelset Congress (IWC), pp. 8-11, Chicago, IL, USA, May 2023
[8] K. Handa, F. Morimoto, “Influence of wheel/rail tangential traction force on thermal cracking of railway wheels”, Wear, v. 289, p. 112-118, 2012.
[9] M. Zálešák, L. Klimeš, P. Charvát, M. Cabalka, J. Kůdela, T. Mauder, “Solution approaches to inverse heat transfer problems with and without phase changes: A state-of-the-art review”, Energy, v. 278, p. 127974, 2023.
[10] ABAQUS, Abaqus Analysis User’s Manual, Simulia, Dassault Systèmes, Providence, RI (USA), 2019.
[11] G.H. Golub, P.C. Hansen, D.P. O’Leary, “Tikhonov regularization and total least squares”, SIAM journal on matrix analysis and applications, v. 21, n. 1, p. 185-194, 1999.
[12] L.T. Biegler, “Large-scale PDE-constrained optimization: an introduction. In: Large-scale PDE-constrained optimization”, Berlin, Heidelberg: Springer Berlin Heidelberg, 2003. p. 3-13.
[13] T. Vernersson, “Temperatures at railway tread braking, Part 1: Modelling”, IMechE: Journal of Rail and Rapid Transit, 221(2):167–182, 2007.
[14] E.G. Birgin, J.M. Martinez, “Practical augmented Lagrangian methods for constrained optimization”, Society for Industrial and Applied Mathematics, 2014.
[15] J. Nocedal, S.J. Wright, Numerical optimization, New York, NY: Springer New York, 2006.